ELSEVIER

Contents lists available at ScienceDirect

Ceramics International

journal homepage: www.elsevier.com/locate/ceramint





Additive manufacturing-assisted sintering: Low pressure, low temperature spark plasma sintering of tungsten carbide complex shapes

Thomas Grippi ^{a,*}, Elisa Torresani ^a, Andrii L. Maximenko ^a, Eugene A. Olevsky ^{a,b}

- ^a Mechanical Engineering, San Diego State University, San Diego, CA, USA
- ^b Nano-Engineering, University of California, San Diego, La Jolla, USA

ARTICLE INFO

Handling editor: P. Vincenzini

Keywords: Tungsten carbide Sintering modeling Spark plasma sintering Additive manufacturing Finite element model

ABSTRACT

Tungsten carbide (WC), renowned for its exceptional hardness and wear resistance, plays an essential role in various industrial applications (cutting tools, abrasives, and wear-resistant components). While traditional methods involve hot pressing, Spark Plasma Sintering (SPS) combined with Additive Manufacturing (AM) offers a cutting-edge approach, utilizing high-voltage electric current and mechanical pressure for rapid densification, particularly advantageous for fabrication of complex shape components made from challenging materials like nanosized binderless tungsten carbide. The study encompasses the entire spectrum of the powder's characterization, extending to the development of an intricate finite element simulation tailored for SPS sintering. Sintering cycles underscore the exceptional quality of the powder, demonstrating full density microstructures even under low-temperature (1550 °C) and low-pressure (50 MPa) conditions. The nanosized powder exhibits minimal microstructural coarsening, reflecting the high quality of the initial pure tungsten carbide nano powder. The core of this study revolves around the methodology employed for deriving constitutive parameters, following the Skorohod-Olevsky theory of continuum sintering. The derivation methods include variations in temperature, heating regimes, and stepwise pressure application during SPS. Additionally, a grain growth model is formulated based on microstructural analysis. Critical parameters, including the apparent sintering activation energy (800 kJ/mol) and the creep law stress exponent (n = 4.0), are discussed. The article concludes with the integration of the mechanical sintering model into finite element method (FEM) software, considering thermal and electrical aspects for a comprehensive SPS-AM modeling approach and its application to complex shape production. The research aims to enhance the understanding of SPS for tungsten carbide, providing insights for its application in manufacturing cutting-edge components in challenging environments.

1. Introduction

Tungsten carbide, a formidable and versatile material, stands at the forefront of modern engineering and manufacturing due to its exceptional hardness, wear resistance, and thermal stability. Comprising tungsten (W) and carbon (C) in equal parts, or often with a metallic additive such as cobalt (Co), tungsten carbide exhibits remarkable properties that have elevated it to a pivotal role in numerous industrial applications [1–3]. In the context of cemented carbides, the impact of grain growth inhibitors is intricately connected to their dissolution in the liquid phase [4]. In parallel to additives such as Cobalt, Vanadium carbide (VC) is often used as a grain growth inhibitor in the sintering of tungsten carbide (WC) [5,6]. The addition of vanadium carbide serves several purposes in the sintering process, contributing to the

improvement of the final properties of the tungsten carbide material. Nevertheless, the inclusion of metallic binders typically leads to a decrease in hardness and compromises corrosion/oxidation resistance [7]. While conventional hardmetals achieve densification through liquid phase sintering at approximately 1350 °C, binderless hardmetals necessitate higher sintering temperatures, typically ranging from 1700 °C to 2000 °C [7].

Renowned for its hardness approaching that of diamonds, tungsten carbide is a key player in the production of cutting tools, abrasives, and wear-resistant components. Its unique combination of toughness and strength allows for the creation of tools that endure extreme conditions, making it indispensable in industries ranging from mining and machining to oil and gas exploration. Tungsten carbide sintering is a sophisticated manufacturing process crucial in producing components for various industrial applications, including cutting tools, wear-

E-mail address: tgrippi@sdsu.edu (T. Grippi).

^{*} Corresponding author.

Nomenclature		$\dot{arepsilon}_{eq}$	Equivalent stain rate
		σ_{eq}	Equivalent stress tensor
0	Density	Ψ	Bulk modulus
o_w	Density of water	φ	Shear modulus
W_1	Dry weight	θ	Porosity
W_2	Weight impregnated with oil	τ	Stress invariant
W_3	Weight of the impregnated sample in water	P	Applied pressure
D_{f}	Final density	γ	Shear strain rate
h_{f}	Final height	ė	Volumetric strain rate
h _t	Height at the specific time t	P_l	Laplace stress
D _t	Density at the specific time t	<u>σ</u>	External stress tensor
G	Mean grain size	$\dot{\underline{arepsilon}}$	External strain rate tensor
n	Creep law stress exponent	k_0	Grain growth pre-exponential factor
A_0	Deformability pre-exponential factor	Q_G	Grain growth activation energy
G	Grain size	$ ho_c$	Critical density
G_0	Initial grain size	R	Gas constant
m	Grain growth exponent	\dot{T}	Heating rate
Q	Apparent sintering activation energy	В	Kinetic field method linearization y-intercept constant
θ	Porosity		
Г	Temperature		

resistant parts, and tools for machining and drilling in challenging environments [8].

In the past, the primary methods for producing fully dense WC ceramics were hot pressing or hot isostatic pressing (HIP) [9]. The use of Spark Plasma Sintering (SPS) for pure tungsten carbide makes perfect sense in a context of sintering this challenging material from nanosized binderless powder while keeping a fine microstructure [7,8]. Alongside tungsten carbide, other challenging carbides sintering via SPS have also been studied to date such as zirconium carbide (ZrC) [10] and tantalum carbide [11].

SPS is a cutting-edge material processing technique that combines high-voltage electric current and uniaxial mechanical pressure to drive the densification and consolidation of powdered materials [12–15]. Its distinctive capability lies in swift densification of materials that traditionally pose challenges for sintering, such as carbides and other high-temperature systems that struggle to achieve high density through conventional sintering methods [16]. The rapid heating rates it achieves are particularly advantageous in preventing excessive grain growth, making it an ideal sintering method for nanosized powders and facilitating the production of structural ceramics, including tungsten carbide.

The development of SPS toward the direction of intricate-shaped components production has been extensively documented. This progress spans from employing specialized tooling to minimize temperature inhomogeneity [17] to the design for simultaneous production of complex parts [18]. In recent years, Additive Manufacturing has demonstrated significant utility in creating sacrificial molds for SPS applications involving complex shapes [19,20]. The technique outlined in this study integrates a stereolithography (SLA)-printed mold of complex geometry with sacrificial powder to ensure sintering homogeneity and shape preservation [21]. Subsequently, the polymeric printed mold is eliminated through outgassing during an initial SPS run conducted at low temperatures (below 600 °C).

Consequently, there is a substantial need for process modeling to comprehend the impact of various SPS parameters on the densification and ultimate microstructure of WC ceramics. This study outlines the essential methodology required to formulate a comprehensive SPS sintering model, in the present case with low pressure (50 MPa) and low sintering temperature (1550 °C). Following a concise overview of conducted studies, characterization methods, and dilatometry curve processing, the article delves into deriving constitutive parameters based on the theory of continuum sintering [22]. Several other models exist [23] from Skorohod-Olevsky [22], Abouaf [24,25], Kraft and Riedel [26] to

viscous poisons ratio form [27,28].

The derivation methods outlined in this research are based on isothermal cycles at different temperatures, variations in heating regimes, and a stepwise approach to applying SPS pressure [29–32]. To achieve the most comprehensive simulation of sintering, a grain growth model is developed using microstructural analysis, along with the derivation of parameters for the grain growth model [12,33].

In conclusion, the article addresses the integration of such a mechanical sintering model into finite element method (FEM) software, considering thermal and electrical aspects for a thorough SPS modeling.

2. Materials and methods

2.1. Methods

2.1.1. Material processing and characterization

The studied material is a commercial powder of tungsten carbide (Cerion Nanomaterials, Rochester, NY).

Size and shape of the powder can be characterized from the Scanning Electron Microscopy images in Fig. 1 left and right (FEI Quanta 450 FEG). It is composed of spherical particles with an average diameter of 104 nm (Fig. 1 left). The Particle size analysis performed via wet method on Anton Paar PSA 1090 in Fig. 1 (right) does not reflect the actual powder size distribution since nanosize powder are in the limits of such device. The particles agglomerates have a identified distribution parameters of $D_{10}=0.11~\mu m$, D_{50} 0.46 μm and $D_{90}=4.27~\mu m$ with a mean size value of 1.36 μm .

The initial powder density has been measured by pycnometry via a helium pycnometer Anton Paar Ultrapyc 5000. The measured initial density of 15,574 kg m $^{-3}$ is reasonably close from the binderless tungsten carbide theoretical one 15,630 kg m $^{-3}$ [34]. The agglomeration of nanosize powder and precision of the device in these conditions are also factors to consider. Results from the Energy Dispersive X-ray Spectroscopy analysis on different zones of the initial powder confirmed the pure tungsten carbide powder without additives (Fig. 2). The studied powder also shows relatively low oxidation with 2.76 wt%.

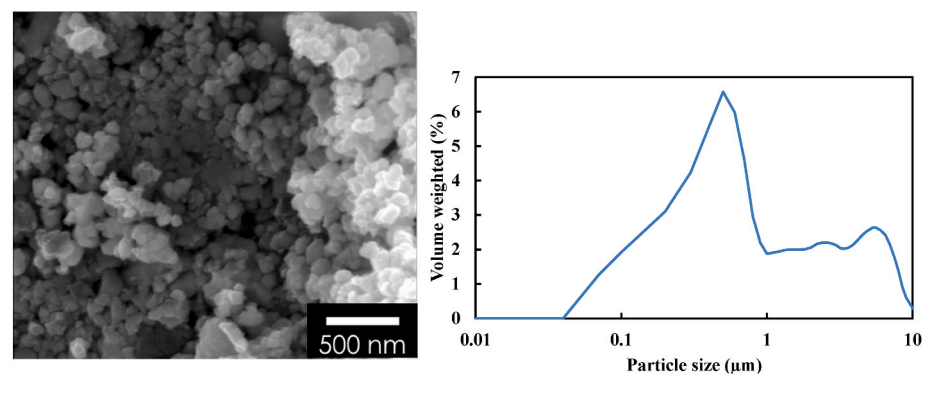


Fig. 1. SEM of the initial powder at magnification ×45k (left) and particle size distribution of the tungsten carbide powder (right).

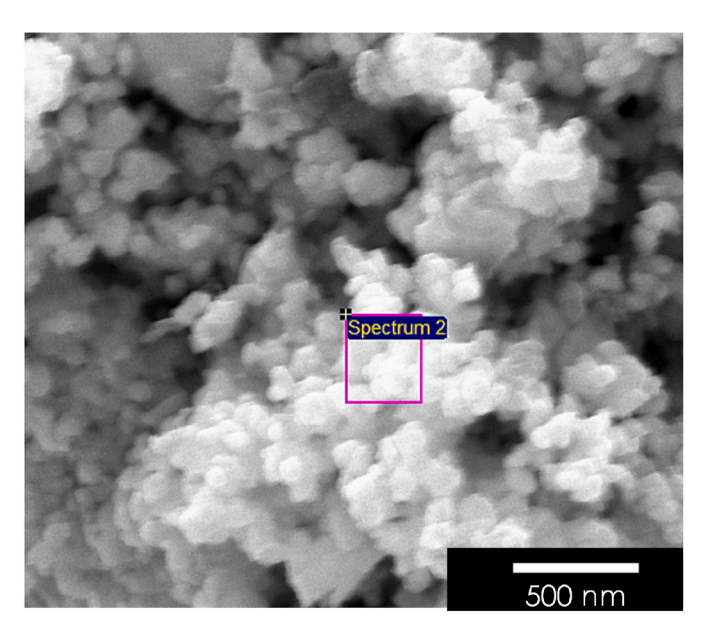


Fig. 2. SEM micrographs and EDS analysis performed on the original powder.

2.1.2. Methods for samples preparation

For all the sintering studies listed in the first part of this report, 12 g of Cerion Nanomaterials WC powder have been prepared in a 15 mm diameter graphite die. Contacts between the die, the punches and the powder were made by graphite foil. All the experiments performed on an SPS machine SPSS DR. SINTER Fuji Electronics model 515. Temperature is regulated by a embedded PID via infra-red pyrometry with Chino IR-AHS. Preliminary studies at sintering temperature 1100 $^{\circ}\text{C}$ and 1200 $^{\circ}\text{C}$ are using a Thermocouple type K.

2.1.3. Method for measurements post-sintering

Samples were measured by a 3 weighing Archimedes method [35].

$$\rho = \frac{W_1 \rho_w}{W_2 - W_3} \tag{1}$$

with ρ the sample density, ρ_w the density of water, W_1 the dry weight, W_2 the weight impregnated with oil and W_3 the weight of the impregnated sample in water.

2.2. Experimental results

Dilatometry data issued from the SPS are vertical displacement as

function of time and temperature. The density evolution during the thermal cycle in a die compacting can be calculated from the expression:

$$\rho_t = \frac{\rho_f}{h_t} h_f \tag{2}$$

with ρ_f the final density, h_f the final height, h_t and ρ_t the height and the density at the specific time t, respectively.

Measurements on samples from the different conducted studies have been gathered in Table 1. The final height and density values are taken as reference for the evaluation of the relative density as function of the time with Equation (1). Without experiencing problematics of thermal runaway or important local melting, very few experiment have been necessary for preliminary characterization.

2.2.1. Preliminary studies

As can be inferred from Table 1, first studies conducted at $1100\,^{\circ}\mathrm{C}$ and $1200\,^{\circ}\mathrm{C}$ shows a minimal densification for cycles with a heating rate of 50 $^{\circ}\mathrm{C}$ /min without holding, under a constant pressure of 50 MPa. These densification data are too negligible to be considered in further parameters derivation. However, the cycle up to $1550\,^{\circ}\mathrm{C}$ in similar conditions shows acceptable densification even without holding (Fig. 3). This temperature will be kept as referential for the following study, with a temperature holding of $15\mathrm{min}$ and a pressure of $50\mathrm{\ MPa}$.

2.2.2. Variations on the heating rates

A study based on several sintering cycles with different heating rates has been carried out for the maximal temperature of 1550 $^{\circ}$ C and the die compaction pressure of 50 MPa. Results from a range of thermal cycles with heating rates between 25 $^{\circ}$ C/min and 100 $^{\circ}$ C/min are displayed in Fig. 4. The data processing shows almost full densification for every cycle with 96.2%, 97.4% and 96.0% of final relative density for 25 $^{\circ}$ C/min, 50 $^{\circ}$ C/min and 100 $^{\circ}$ C/min respectively.

Literature reports similar sintering heating rates for SPS of WC components with dopants but usually lower sintering temperature such as $1100\,^{\circ}\text{C}$ or $1200\,^{\circ}\text{C}$ depending on the cobalt concentration [7,16,36, 37]. Nevertheless, the sintering temperature of $1550\,^{\circ}\text{C}$ remains low for this typical component under such low pressure [7,9].

On the other hand, based on accurate and almost fully dense samples data, the derivation of a first range of constitutive parameters for a sintering simulation is now possible. This will be at the heart of the *data* processing and modeling part of this document.

2.3. Data processing and modeling

2.3.1. Model description

Adhering to the continuum theory of sintering [22], the investigated samples can be viewed as exhibiting a dense phase behavior rooted in creep. The equations governing equivalent stress and strain rate conform to the Norton creep law.

 Table 1

 Specimen measurements post-sintering and their corresponding cycles.

Cycle	Final height (mm)	Final radius (mm)	Weight (g)	Bulk density from dimensions	Bulk density from Archimede	Relative density from dimensions	Relative density from Archimede
1100 °C for 15 min, 50 Mpa, 50 °C/min	7.68	15.00	11.31	8.33	-	53.5%	-
1200 °C for 15 min, 50 Mpa, 50 °C/min	7.50	15.00	12.08	9.11	-	58.5%	-
1550 °C for 0 min, 50 Mpa, 50 °C/min	4.74	15.00	11.80	14.09	14.20	90.5%	91.2%
1550 °C for 15 min, 50 Mpa, 50 °C/min	3.61	15.00	9.70	15.23	15.17	97.8%	97.4%
1550 °C for 15 min, 50 Mpa, 100 °C/min	3.76	15.00	9.84	14.83	14.95	95.2%	96.0%
1550 °C for 15 min, 50 Mpa, 25 °C/min	3.72	15.00	9.88	15.02	14.98	96.4%	96.2%
1550 °C for 15 min, pressure variations, 50 °C/min	3.65	15.00	9.49	14.71	14.89	94.4%	95.6%
1550 °C then 1500 °C for 15 min, 50 MPa, 50 °C/min	3.81	15.00	9.73	14.45	14.60	92.8%	93.7%

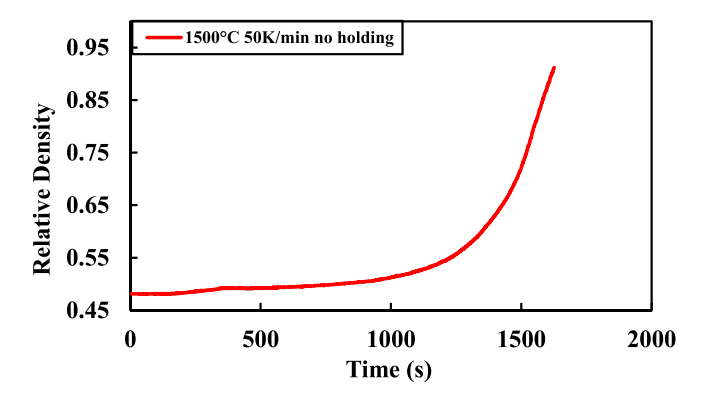


Fig. 3. Relative density as fucntion of sintering time for the SPS sintering of WC component.

$$\dot{\varepsilon}_{eq} = A(T, G)\sigma_{eq}^{n} = A_0 \left(\frac{G_0}{G}\right)^m \frac{\exp\left(\frac{-Q}{RT}\right)}{T}\sigma_{eq}^{n} \tag{3}$$

With n the creep law stress exponent, A_0 the deformability preexponential factor, G the grain size, G_0 the initial grain size, m the grain growth exponent, Q the apparent sintering activation energy and Tthe temperature.

Equivalent stain rate and stress tensors are defined as:

$$\dot{\varepsilon}_{eq} = \frac{1}{\sqrt{1-\theta}} \sqrt{\varphi \dot{\gamma}^2 + \psi \dot{e}^2}$$
 (4)

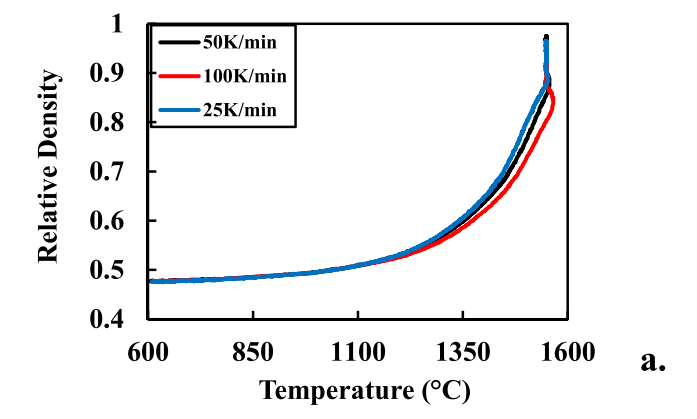
$$\sigma_{eq} = \frac{\sqrt{\frac{r^2}{\varphi} + \frac{(P - P_f)^2}{\psi}}}{\sqrt{1 - \theta}} \tag{5}$$

where φ and ψ are respectively shear and bulk moduli, functions of the porosity θ . Terms τ , P, $\dot{\gamma}$ and \dot{e} are the stress and strain rate invariants defined below.

$$\tau = \frac{\sqrt{(\sigma_{x} - \sigma_{y})^{2} + (\sigma_{y} - \sigma_{z})^{2} + (\sigma_{z} - \sigma_{x})^{2} + 6(\sigma_{xy}^{2} + \sigma_{yz}^{2} + \sigma_{xz}^{2})}}{\sqrt{3}}$$
(6)

$$P = \frac{\sigma_x + \sigma_y + \sigma_z}{3} = \frac{I_1}{3} \tag{7}$$

$$\dot{\gamma} = \sqrt{2\left(\dot{\varepsilon}_{xy}^2 + \dot{\varepsilon}_{xz}^2 + \dot{\varepsilon}_{yz}^2\right) + \frac{2}{3}\left(\dot{\varepsilon}_x^2 + \dot{\varepsilon}_y^2 + \dot{\varepsilon}_z^2\right) - \frac{2}{3}\left(\dot{\varepsilon}_x\dot{\varepsilon}_y + \dot{\varepsilon}_x\dot{\varepsilon}_z + \dot{\varepsilon}_y\dot{\varepsilon}_z\right)}$$
(8)



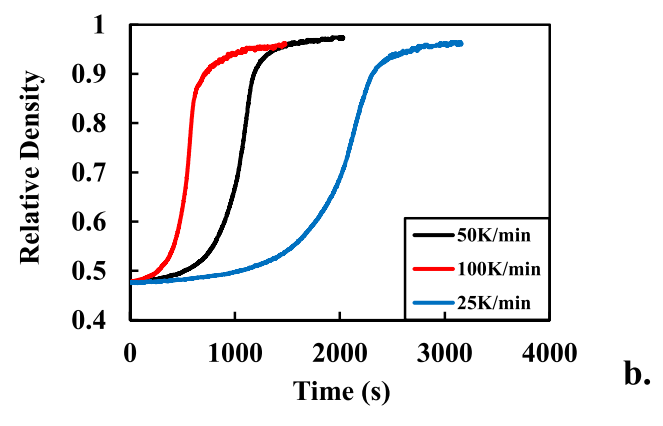


Fig. 4. Relative density as a function of temperature (b.) and time (a.) for thermal cycle at 1550 $^{\circ}C$ and heating rates variation 25 $^{\circ}C/min$, 50 $^{\circ}C/min$ to 100 $^{\circ}C/min$.

$$\dot{e} = \dot{\varepsilon}_x + \dot{\varepsilon}_y + \dot{\varepsilon}_z \tag{9}$$

The term P_l represents the Laplace stress arising from particle capillarity forces. These forces can be defined by the particle radius and the porosity, as per the principles outlined in Skorohod-Olevsky theory [22,38].

$$P_l = \frac{3\alpha}{r} (1 - \theta)^2 \tag{10}$$

In the context of the current Spark Plasma Sintering (SPS) scenario, the

capillarity forces can be considered negligible in comparison to the applied stress ($P_1 \ll \sigma_z$). The following mass conservation law establishes a connection between the rate of porosity elimination and the rate of volume change:

$$\frac{\dot{\theta}}{(1-\theta)} = \dot{e} \tag{11}$$

Finally, the general sintering behavior of a continuum can be defined as:

$$\underline{\sigma} = \frac{\sigma_{eq}}{\dot{\varepsilon}_{eq}} \left(\varphi \underline{\dot{\varepsilon}} + \left(\psi - \frac{1}{3} \varphi \right) \dot{e}^{\dagger} \right) + P_l \ddot{\iota}$$
(12)

2.3.2. Specific case for SPS

Spark Plasma Sintering can be likened to a high-temperature die pressing test conducted along the z-axis. The external strain rate tensor can be simplified to:

$$\underline{\dot{\varepsilon}} \equiv \begin{pmatrix} 0 & 0 & 0 \\ 0 & 0 & 0 \\ 0 & 0 & \dot{\varepsilon}_z \end{pmatrix}$$
(13)

By the use of graphite foil interface, the lateral friction is considered negligible.

Based on equation (11), we can simplify.

$$\dot{e} = \dot{\varepsilon}_z, \dot{\gamma} = |\dot{\varepsilon}_z| \sqrt{\frac{2}{3}}, \dot{\varepsilon}_{eq} = |\dot{\varepsilon}_z| \sqrt{\frac{\psi + \frac{2}{3}\varphi}{1 - \theta}}, \tag{14}$$

With combination of equations (4) and (12)–(14) the stress z σ_z term is:

$$\sigma_{z} = \frac{\dot{\varepsilon}_{eq}^{\frac{1}{n}-1}}{A(T,G)^{\frac{1}{n}}} \left(\varphi \dot{\varepsilon}_{z} + \left(\psi - \frac{1}{3} \varphi \right) \dot{\varepsilon}_{z} \right)$$
(15)

The analytical SPS equation is then:

$$|\dot{\varepsilon}_z| = A_0 \left(\frac{G_0}{G}\right)^m \frac{\exp\left(\frac{-Q}{RT}\right)}{T} \left(\psi + \frac{2}{3}\varphi\right)^{\frac{-n-1}{2}} (1-\theta)^{\frac{1-n}{2}} |\sigma_z - P_l|^n$$
 (16)

With ψ and φ the normalized shear and bulk viscosity moduli expressed as:

$$\psi = \frac{2}{3} \frac{(1-\theta)^3}{\theta} \text{ and } \psi = (1-\theta)^2$$
 (17)

From equation (16), the constitutive parameters to be determined are then the creep law stress exponent n, the activation energy Q and the pre-exponential factor A_0 .

2.3.3. Derivation of the creep law stress exponent: n

In this section, the stress exponent n is derived. The approach, grounded in the analytical equations explained earlier, mirrors the procedure outlined in the publications by Maniere et al. [39] and Li et al. [30]. The methodology entails executing targeted "pressure jumps" while holding the temperature constant. In this specific context, the technique is utilized to ascertain the exponent "n" by examining the alteration in the sintering shrinkage rate before and after the pressure "jump." It is imperative for the sudden pressure shift to be rapid enough to forestall substantial fluctuations in relative density.

From Equation (16) we can isolate n terms:

$$|\dot{\varepsilon}_z| = A \frac{\sqrt{1-\theta}}{\sqrt{\psi + \frac{2}{3}\varphi}} \left(\frac{\sigma_z}{\sqrt{1-\theta}\sqrt{\psi + \frac{2}{3}\varphi}} \right)^n \tag{18}$$

If the pressure jumps of the stepwise approach implies no porosity variation, the strain rate ratio before and after the pressure variation simplify all the porosity dependent terms. The formulation (18) is thus simplified to:

$$n = \frac{\ln\left(\frac{\dot{\epsilon}_1}{\dot{\epsilon}_2}\right)}{\ln\left(\frac{\sigma_1}{\sigma_2}\right)} \tag{19}$$

In the other hand, if the pressure transition implies a porosity evolution which is not negligible, the strain rate ratio can be expressed:

$$\frac{\dot{\varepsilon}_{1}}{\dot{\varepsilon}_{2}} = \frac{\sqrt{1 - \theta_{1}} \sqrt{\psi_{2} + \frac{2}{3}\varphi_{2}}}{\sqrt{1 - \theta_{2}} \sqrt{\psi_{1} + \frac{2}{3}\varphi_{1}}} \left(\frac{\sigma_{1}\sqrt{1 - \theta_{2}} \sqrt{\psi_{2} + \frac{2}{3}\varphi_{2}}}{\sigma_{2}\sqrt{1 - \theta_{1}} \sqrt{\psi_{1} + \frac{2}{3}\varphi_{1}}} \right)^{n}$$
(20)

By isolating the n term and taking the logarithm we thus have:

$$\ln \left(\frac{\frac{\dot{e}_{1}}{\dot{e}_{2}} \frac{\sqrt{1-\theta_{2}}\sqrt{\psi_{1} + \frac{2}{3}\varphi_{1}}}{\sqrt{1-\theta_{1}}\sqrt{\psi_{2} + \frac{2}{3}\varphi_{2}}} \right) \\
n = \frac{1}{\ln \left(\frac{\sigma_{1}}{\sigma_{2}} \frac{\sqrt{1-\theta_{1}}\sqrt{\psi_{2} + \frac{2}{3}\varphi_{2}}}{\sqrt{1-\theta_{2}}\sqrt{\psi_{1} + \frac{2}{3}\varphi_{1}}} \right)} \right) \tag{21}$$

The derivation method for Equation (21), accounting for slight porosity evolution and varying strain rates, is depicted in Fig. 5.

In the experimental work, 4 pressure jumps of 10 MPa have been performed from 37 MPa to 77 MPa. Each holding step has last 2 min with a 10s stepwise pressure application. This has been conducted during a temperature holding at 1550 °C from a heating rate of 50 °C/min. Fig. 6 presents the load variation from which is calculated the applied pressure expressed in Equation (21). From data at each pressure jumps with a slight density variation (as illustrated in Fig. 5), the mean parameter n is identified to be n = 4.0. This derived value infers a dislocation climb controlled by diffusion as the consolidation mechanism. Literature reports similar values with 3-4 measured by Smith et al. [40] and 4-5 for this tungsten carbide component with cobalt dopant reported by S. Lay et al. [41]. In the latter publication is reported that this creep exponent parameter should only be function of the volume concentration of cobalt. With a n that should tends to 1 for a pure tungsten carbide. The powder nano size might also have an influence on this parameter hence the divergence from typical values found in literature.

2.3.4. Derivation of the activation energy: Q

In a first hand, the variation on the heating rate is meant to be used as data for an identification of the apparent sintering activation energy via methods as the master sintering curve (MSC) [32,42] or kinetic fields [43–45]. In the present case, analyzing data within a limited experimental anisothermal zone may introduce potential biases to the results. Considering this, the research group has chosen to begin with an isothermal method for this study, and the subsequent section elaborates on its application in deriving the activation energy. In light of this, the group has opted for an isothermal method in this study, and its application for deriving the activation energy is discussed in the following section.

2.3.4.1. Isothermal method for sintering apparent activation energy derivation. As outlined in the study by Maniere et al. [24], the determination of the activation energy Q for the creep law involves conducting tests at various holding temperatures. Formulating from the analytical expressions (11) and (16), we can derive:

$$\left|\frac{\dot{\theta}}{(1-\theta)}\right| = A_0 \left(\frac{G_0}{G}\right)^m \frac{\exp\left(\frac{-Q}{RT}\right)}{T} \sigma_{eq}^n \left(\psi + \frac{2}{3}\varphi\right)^{\frac{-n-1}{2}} (1-\theta)^{\frac{1-n}{2}} |\sigma_z|^n$$
 (22)

For two Spark Plasma Sintering (SPS) compaction tests conducted

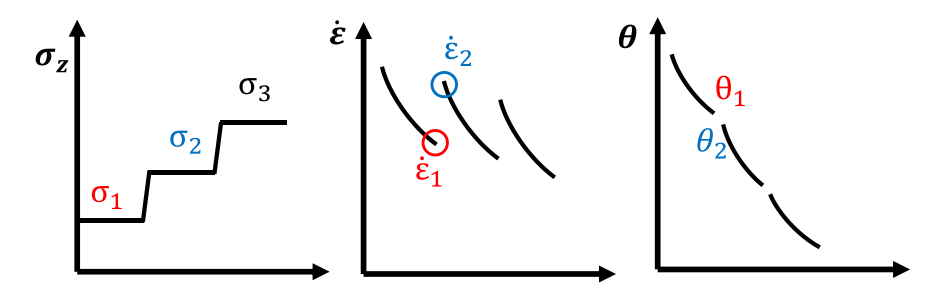


Fig. 5. Schematic of the stepwise approach in the case of slight porosity evolution () $\theta_1 > \theta_2$).

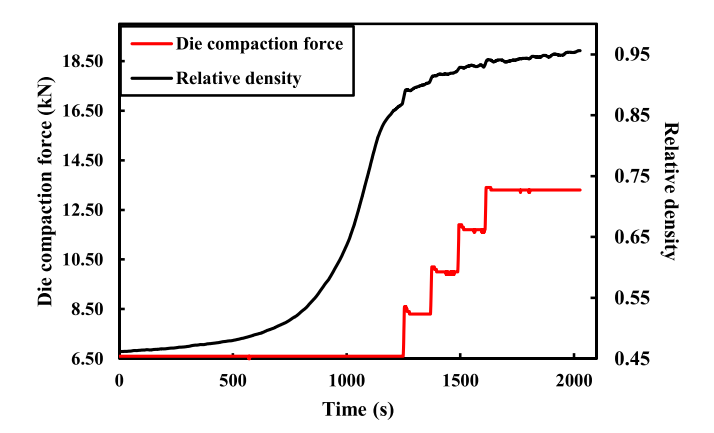


Fig. 6. Measured die compaction force (red) and relative density of the studied specimen as a function of time during a 1550 $^{\circ}$ C temperature holding.

under identical applied stress σ_z and porosity θ , yet at different temperature holding, the relationship can be expressed as follows:

$$\left| \frac{\dot{\theta}_1}{\dot{\theta}_2} \right| \frac{T_1}{T_2} = \frac{\exp\left(\frac{-Q}{RT_1}\right)}{\exp\left(\frac{-Q}{RT_2}\right)} = \exp\left(\frac{Q}{R}\left(\frac{1}{T_2} - \frac{1}{T_1}\right)\right)$$
 (23)

Apparent sintering activation energy Q can be isolated:

$$Q = \frac{Rln\left(\frac{\dot{\theta_1}}{\dot{\theta_2}}\frac{T_1}{T_2}\right)}{\frac{1}{T_1} - \frac{1}{T_1}} \tag{24}$$

The experimental work involved the execution of two comparable Spark Plasma Sintering (SPS) thermal cycles, both employing a 50 MPa pressure and a heating rate of 50 °C/min. The first cycle was conducted at 1550 °C for 15 min (depicted in black in Fig. 7), while the second cycle

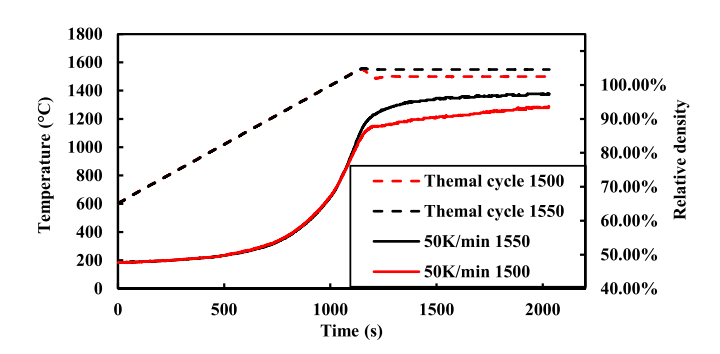


Fig. 7. Thermal cycles and relative density as function of the time for cycles at 1550 $^{\circ}$ C for 15min (in black) and cycle at 1550 $^{\circ}$ C then 1500 $^{\circ}$ C for 15min (in red).

took place at 1500 $^{\circ}$ C for 15 min following a peak temperature of 1550 $^{\circ}$ C, as illustrated in red in Fig. 7 below. Subsequently, utilizing equation (24) and the gathered experimental data, the activation energy Q was determined for relative density ranging from 90% to 92%, with an identified value of 800 kJ/mol.

Seemingly, the identified parameter is slightly higher than values related in literature. The latter relates sintering activation energy for similar components around 201–282 kJ/mol from V·N.Chuvil'deev et al. [46]. J.T. Smith et al. [40] reported lowered sintering activation energies by the mean of cobalt additives of 220 kJ/mol. Values of 412–433 kJ/mol were derived by G. Lee et al. with temperature cycle ranging from 1600 °C to 1800 °C for pure tungsten component [47]. Finally, dense tungsten carbide produced in the sintering range of 2100–2500 °C by hot pressing, exhibited an apparent sintering activation energy of 591 kJ/mol [48]. To confirm the identified value in a first hand, the authors have performed a secondary analysis using this time anisothermal activation energy identification methods: the Master sintering curve [49] and the kinetic field method described by Wang & Raj [43].

2.3.4.2. Master sintering curve. The master sintering curve method has been performed on densification data from 25 °C/min, 50 °C/min and 100 °C/min cycles (Fig. 8 top) using the house-made software SINTERLab. The software follows the method from Su et al. [49]. Each of densification curves required the calculation of the Θ parameter by the equation below.

$$\Theta(t,T) \equiv \int_{0}^{t} \frac{\exp\left(-\frac{Q}{RT}\right)}{T} dt \tag{25}$$

To determine the activation energy, a minimization procedure was then conducted between 60%RD and 80%RD (Fig. 8 bottom). Accordingly, the identified parameter is 810 kJ/mol and identification shows a good fit of all points.

2.3.4.3. Kinetic fields approach. The method developed by Wang and Raj [43] is used to linearize the following expression:

$$-\frac{Q}{RT} + B = \ln\left(\frac{d\rho}{dT} \cdot T \cdot \dot{T}\right) \tag{26}$$

With Q the apparent sintering activation energy, T the temperature R the gas constant, ρ the relative density and \dot{T} the heating rate. The term B gathers all sintering model constants, including the applied stress, constant in the use case of both parameters' derivation methods M.S.C. and Kinetic fields. It was employed to assess the convergence with the MSC value and to identify any potential changes in activation energy at various relative densities (Fig. 9). Within the relative-density range of 60–80%, 10 different relative density were linearized, a consistent value of 790 kJ/mol was observed. Both used methods report a relatively close apparent sintering activation energy value 800 kJ/mol.

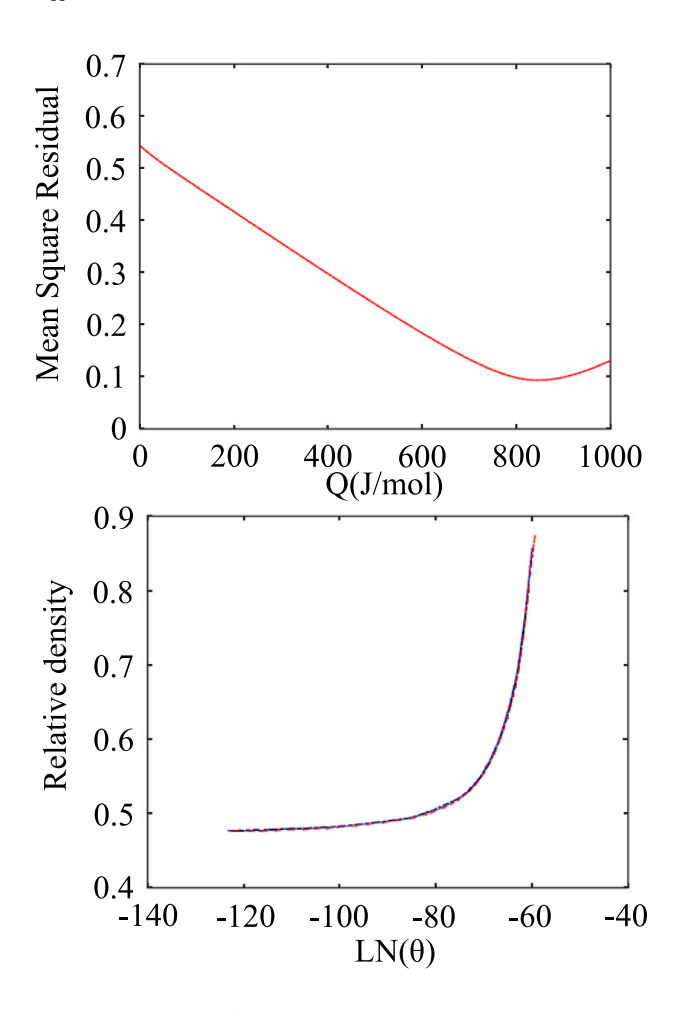


Fig. 8. Identification of the apparent activation energy via master sintering curve method, computation of the error for the MSC for apparent sintering activation energy ranging from 0 to 1000 kJ/mol (top), plot of the MSC for the least error case 810 kJ/mol (bottom).

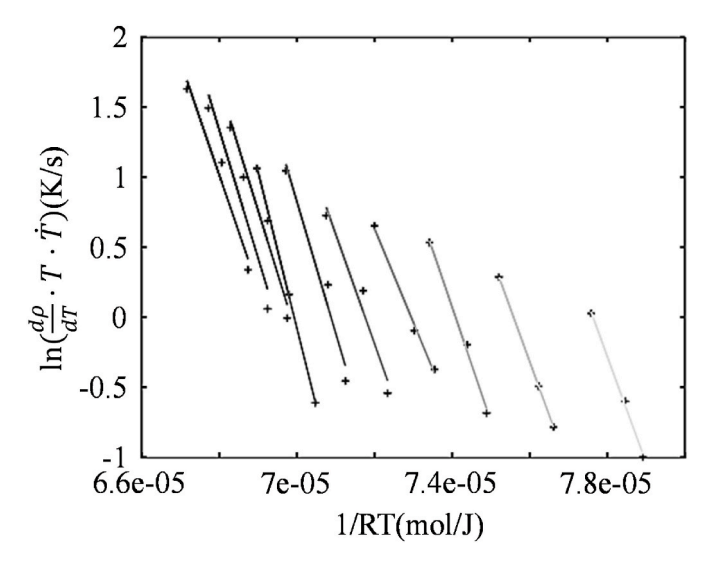


Fig. 9. Identification of the apparent activation energy via kinetic field method.

2.3.5. Grain growth modeling

For the microstructural analysis, sample has been sliced and polished before SEM observation (FEI Quanta 450 FEG). No etching has been performed and the microstructure revealed clearly with backscattered electron detector (Fig. 10). From dense sample after a cycle at 1550 $^{\circ}\mathrm{C}$ for 15min after a 50 $^{\circ}\mathrm{C/min}$ heating rate the microstructure presents granular microstructure with a few porosities.

From micrographs above grain size has been identified via the linear intercepts method [50].

$$G = \frac{X^*1.56}{N}$$
 (26)

Mean grain size G [m] at final state is calculated from the ratio between the number of grain boundaries X within a line of length N [m] and multiplied with a stereological factor from single-dimensional to tridimensional 1.56. Accordingly, the mean grain size at the final state is 716 nm. This value has been calculated from several micrographs at different zones of the specimen, exhibiting homogeneous grain growth with a limited standard deviation of 27.94 nm. This outcome underscores the great quality of the powder, highlighting an almost full densification without encountering issues like melting or thermal runaway during SPS.

In the present task, the grain growth has been modeled from the experimental data depicted in Section 4, with an initial particle size of 104.8 nm and a final grain size of 716 nm. Grain growth has been modeled from the Olevsky's model (27) describing the grain growth rate as function of relative density and grain size [12].

$$\frac{dG}{dt} = \frac{k_0}{3G^2} \left(\frac{1 - \rho_c}{2 - \rho_c - \rho} \right)^{\frac{3}{2}} exp\left(\frac{-Q_G}{RT} \right)$$
 (27)

From (27) and sintering data following parameters have been fitted, pre-exponential factor ${\bf k}_0=10$ E-8, a grain growth activation energy $Q_G=500$ kJ/mol and a critical density parameter representing the relative density from which the grain growth starts $\rho_c=0.9$ as can be observed below on Fig. 11.

2.3.6. Fitting with linearization for the derivation of A_0

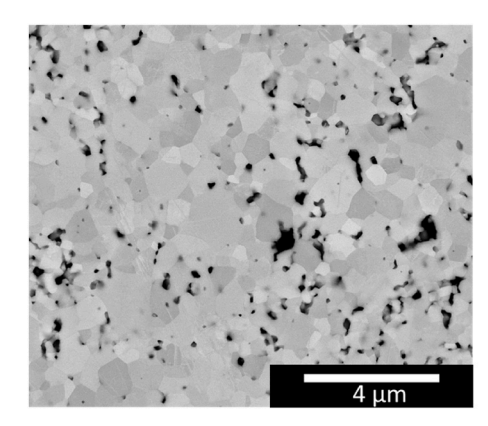
In this step, we derive two specific parameters: the deformability pre-exponential factor A_0 and adjust the bulk modulus $\psi(\theta).$ The determination of A_0 can be achieved through linear regression in the intermediate stage of sintering, as outlined in equation (28). It is crucial to acknowledge that the bulk modulus function might introduce variations in the regression curve, resulting in an activation energy distinct from that derived using the MSC method. Skorohod's theoretical bulk modulus is represented by Eq (16). However, this modulus does not consider the initial sintering phase characterized by heightened reactivity due to point-like particle contacts. Abouaf [51] addressed this by proposing a solution that introduces an initial-stage critical-porosity parameter (θ_{cl}) to model this phenomenon:

$$\psi = \frac{2}{3} \frac{(\theta_{ci} - \theta)^3}{\theta} \tag{28}$$

Following the method depicted by Manière et al. [45,52], the identified initial critical porosity is thus 53%RD. From the mass conservation law (10), Equation (15) can be rearranged and linearized with a logarithm form to isolate Q and A_0 as below [52]:

$$Y = \ln\left(T|\dot{\theta}| \left(\frac{G}{G_0}\right)^m \left(\psi + \frac{2}{3}\varphi\right)^{\frac{n+1}{2}} (1-\theta)^{\frac{n-3}{2}} |\sigma_z - P_l|^{-n}\right) = \ln(A_0) - \frac{Q}{RT}$$
(29)

For the purpose of this study, the reference experimental cycle is "1550 $^{\circ}$ C for 15min, uniaxial pressure of 50 MPa, 50 $^{\circ}$ C/min" where the final relative density has reached 97.4%. In this case the regression is focused in a zone supposed with limited grain growth (see Fig. 12) so the



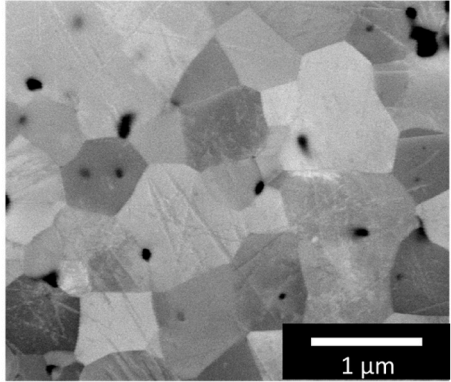


Fig. 10. Secondary electron microscopy micrograph at magnification ×10k (left) back scatterd electron microscopy micrograph at magnification ×29k (right).

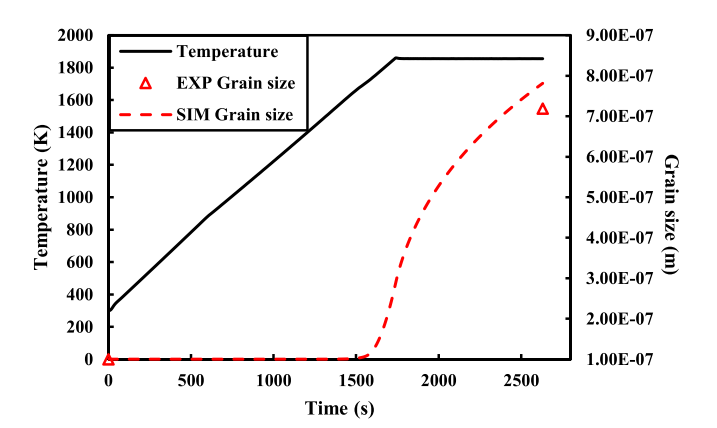


Fig. 11. Simulated mean grain size and temperature as the function of the time in COMSOL Multiphysics.

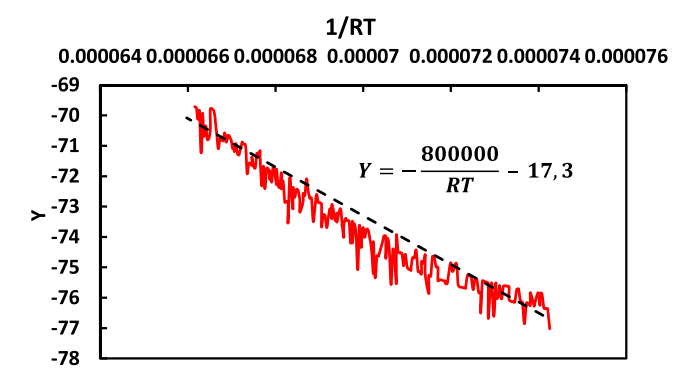


Fig. 12. Linear fitting to derive A_0 from the identified parameter Q with experimental data from cycle 50K/min and 1550 $^{\circ}$ C.

term A is simplified to its formulation:

In this study, the reference experimental cycle is defined as "1550 °C for 15 min, uniaxial pressure of 50 MPa, and heating rate of 50 °C/min," leading to a final relative density of 97.4%. For this particular case, the regression is concentrated within a zone assumed to have limited grain growth (refer to Fig. 12), simplifying the term A to its specific formulation:

$$A(T) = A_0 \frac{\exp\left(\frac{-Q}{RT}\right)}{T} \tag{30}$$

The value of Q is fixed for a linear fitting from the identified value

detailed in the previous part, $800\,kJ/mol$. On its side the identified value for the deformability pre-exponential factor is $A_0=3.067e-8$ (K·s $^{-1}$ Pa $^{-n}$).

3. Results and discussion

3.1. Finite element method modeling

In this part, the mechanical model is implemented in a commercial finite element software, COMSOL Multiphysics. This software enables a coupling of the different physics of the SPS furnace to the mechanical model of sintering to result in a comprehensive electrical-thermal-mechanical simulation. For the purpose of the study the sintering configuration is computed as a 2D axisymmetric model as the geometry shown in Fig. 13.

3.1.1. SPS model implementations

The Spark Plasma Sintering (SPS) model implemented can be conceptualized as a combination of five primary components: the electric current flow, induced Joule heating, surface-to-surface radiation, densification, and grain growth. The first three are addressed for both the SPS tooling and the specimen, while the last two are specifically resolved for the tungsten carbide specimen. The implementation details

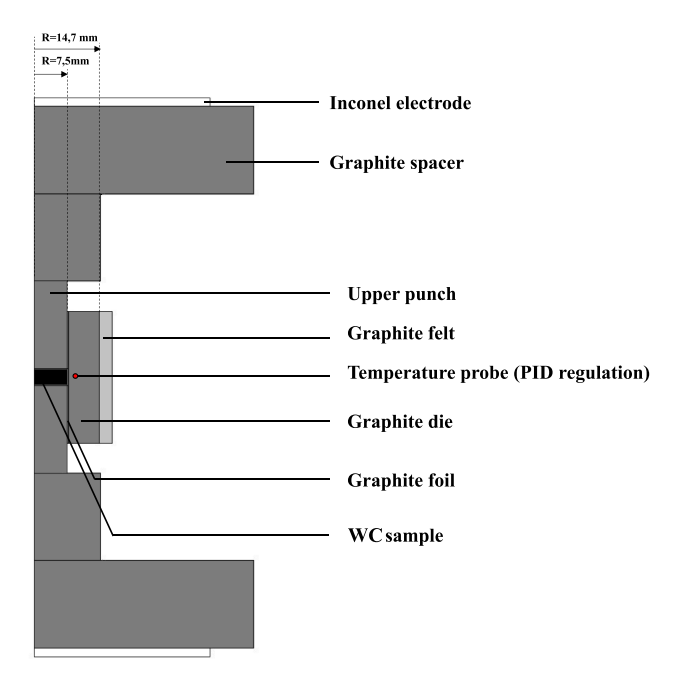


Fig. 13. Axisymmetric geometry for FEM model of SPS.

of these components are extensively documented in the literature [12, 53–56].

Tables 2 and 3 gathers the thermal, mechanical, and electrical properties of the materials employed in the simulation. Parameters for Inconel, graphite, and graphite felt are extracted from literature sources [53,54], while properties for tungsten carbide are obtained from [9,57,58]. Consistent with the SPS simulation in Diatta et al. [54], electrical contact resistance (ECR) data are derived from the work of Wei et al. [59], and thermal contact resistance (TCR) is sourced from the study conducted by Maniere et al. [55].

In the entire tooling, the initial temperature is assumed to be 20 $^{\circ}\text{C},$ and at this state, the electric current density throughout the Spark Plasma Sintering (SPS) tooling is set to zero.

For the mechanical model illustrated in the preceding section, the initial state and boundary conditions are as follows:

- The initial displacement is initialized to zero across the entire tooling.
- Uniaxial pressure is applied to the upper graphite punch, permitting its vertical displacement.
- The lower punch is fixed in the model with no vertical displacement.
- · Other boundaries are defined as free.

As for the electrical boundary conditions, the ground is fixed on the lower electrode with a potential of zero. The current is applied to the upper electrode, and its regulation is accomplished through a PID controller embedded [56], following the provided expression:

$$I(t) = Kpe(t) + K_I \int_0^t e(\tau)d\tau + K_D \frac{de(t)}{dt}$$
(30)

Most suitable parameters for this PID controlling are $K_P = 1500,\, K_{\rm I} = 100$ and $K_{\rm D} = 10.$

3.1.2. Simulation results

The simulated evolution of the mean relative density compared to the experimental data show a good correspondence as shown on Fig. 15. Initial stage experimental data densification at low relative density is mainly related to particles rearrangement, explaining the slight gap between simulation and sample. The presented model with derived parameters is able to predict the densification of the studied specimen.

Fig. 16 gives a more detailed picture of the density distribution during the temperature dwelling at 1550 °C, for the time t=1600s (beginning of the holding), t=2100s and t=2630s (final sintering

Table 2Properties of inconel, graphite, and graphite felt.

Properties	Inconel	Graphite	Graphite felt
Electrical conductivity (S·m ⁻¹)	$1/(1.6 \times 10^{-10} \times T + 9.82 \times 10^{-7})$	$1/(5.81 \times 10^{-16} \times T^3 + 1.29 \times 10^{-12} \times T^2 -9.17 \times 10^{-9} \times T + 1.84 \times 10^{-5})$	333
Thermal conductivity (W⋅m ⁻¹ K ⁻¹)	$-1.57 \times 10^{-2} \times T + 10.09$	$-6.13 \times 10^{-9} \times T^{3} + 3.74 \times 10^{-5} \times T^{2} - 8.55 \times 10^{-2} \times T + 100.05$	For T $<$ 1273 K 2.00 \times 10–7 \times T ² -1.90 \times 10 ⁻⁴ \times T + 0.14 For T $>$ 1273 0.217
Heat capacity (J·kg ⁻¹ K ⁻¹)	$0.250\times T+\\344$	$-9.6 \times 10^{-4} \times T^2 + \\ 2.72 \times T - 34.27$	For T $<$ 1673 K $0.69 \times T + 507.53$ For T $>$ 1673K 1675
Density (kg⋅m ⁻³)	8430	1860	88
Young's modulus (GPa)	400	180	-
Poisson's ratio (–)	0.29	0.262	-
Emissivity (-)	0.67	0.8	0.99

 Table 3

 Properties of tungsten carbide powder as a function of the relative density.

Properties	Tungsten carbide
Electrical conductivity (S·m ⁻¹) [9]	$\left(1 - \frac{3}{2}(1 - \rho)\right) \cdot (2.725 + 04 \times \text{T}'(-8.70448 \times 10^{-1}))/$
Thermal conductivity $(W \cdot m^{-1} K^{-1}) [9]$	$ (2.44E-8 \times T) $ $ \left(1 - \frac{3}{2}(1 - \rho)\right) \cdot (2.725 + 04 \times T^{\circ}(-8.70448 \times 10^{-1})) $
Heat capacity ($J \cdot kg^{-1} K^{-1}$) [57]	$\rho \cdot (8.26329 \times 10^{-2} \times log(T) - 2.49821 \times 10^{-1}) \times 1000$
Young's modulus (GPa) [57]	$\begin{array}{l} (\text{-}2.03655 \times 10^{-7} \times \text{T}^3 + 3.94188 \times 10^{-4} \times \text{T}^2 \text{-}2.89188 \\ \times \ 10^{-1} \times \text{T} + 7.26196 \times 10^2) \times 1 \times 10^9 \cdot \end{array}$
	$\left(rac{ ho}{1+2.13(1- ho)} ight)$
Poisson's ratio (-)	0.22

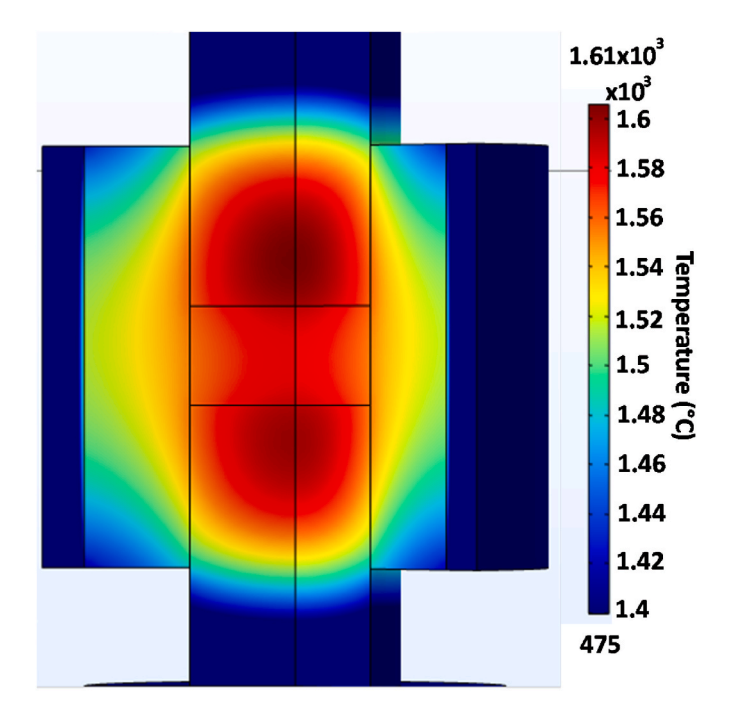


Fig. 14. Cross section of the tooling, temperature distribution of SPS sintering of tungsten carbide at 2630s (Final time of the holding at 1550 $^{\circ}$ C).

time). The density mapping shows a higher densification than the mean value at the top part and bottom parts of the sample, touching the tooling. This density gradient is more important at the holding starting time (1600s) than at the final time. Gradient inferred from a temperature distribution showing higher temperature on these contact zones (up to 0 $^{\circ}$ C on Fig. 14) through the whole cycle. Indeed, this also corroborate the higher grain size as expected on Fig. 15, at the same time steps. Correspondingly to SEM microstructural observations density distribution and grain size remain homogeneous at the last stage of sintering.

3.1.3. Sintering and simulation of intricate geometries shaped with additive manufacturing

Additive manufacturing enables the design and fabrication of sacrificial molds specifically tailored for the sintering process of complex-shaped parts in SPS. Utilizing in parallel to AM the advanced Spark Plasma Sintering model, our team simulated a cupola-shaped sample and conducted a corresponding experiment for comparative analysis. The outcomes of this recent experiment validate the efficacy of the proposed methodology in both predicting and producing intricate shapes with additive manufacturing sacrificial mold and composed of pure tungsten carbide through the Spark Plasma Sintering process.

To sinter the intricate shape detailed in this section, a polymeric

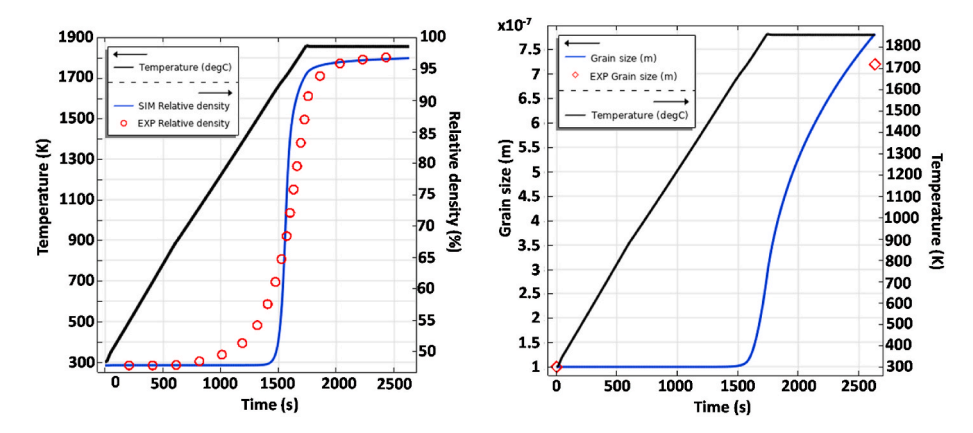


Fig. 15. Thermal cycle and mean grain size as a function of the time and experimental data (left) and simulated mean relative density evolution as a function of the time (right).

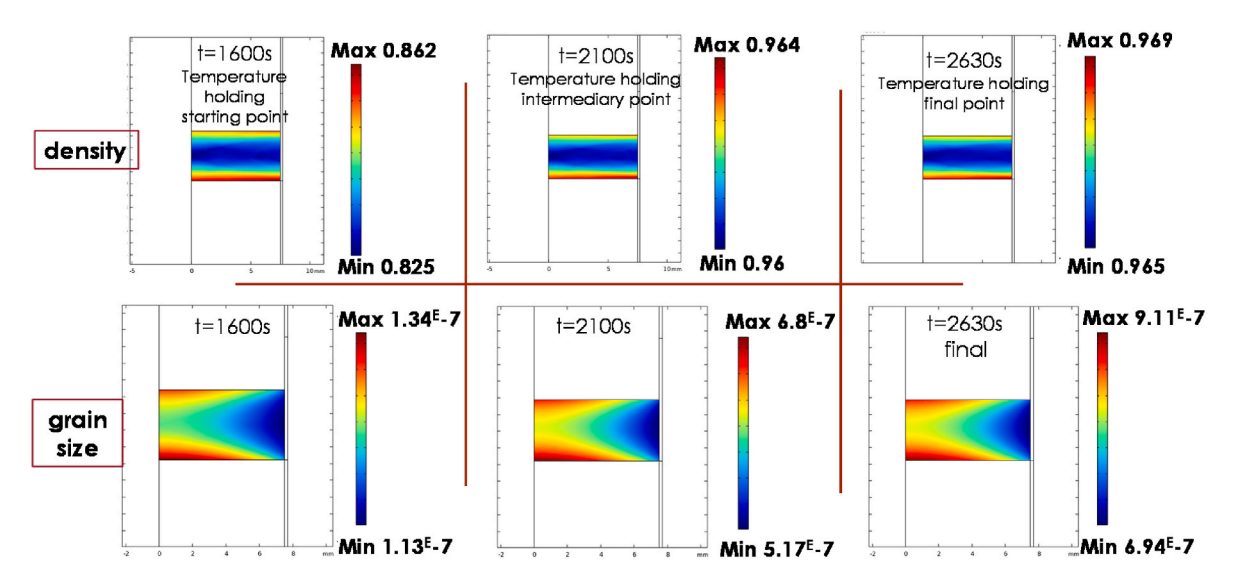


Fig. 16. Density (above) and grain size (below) distributions during the temperature dwelling at 1550 $^{\circ}$ C.

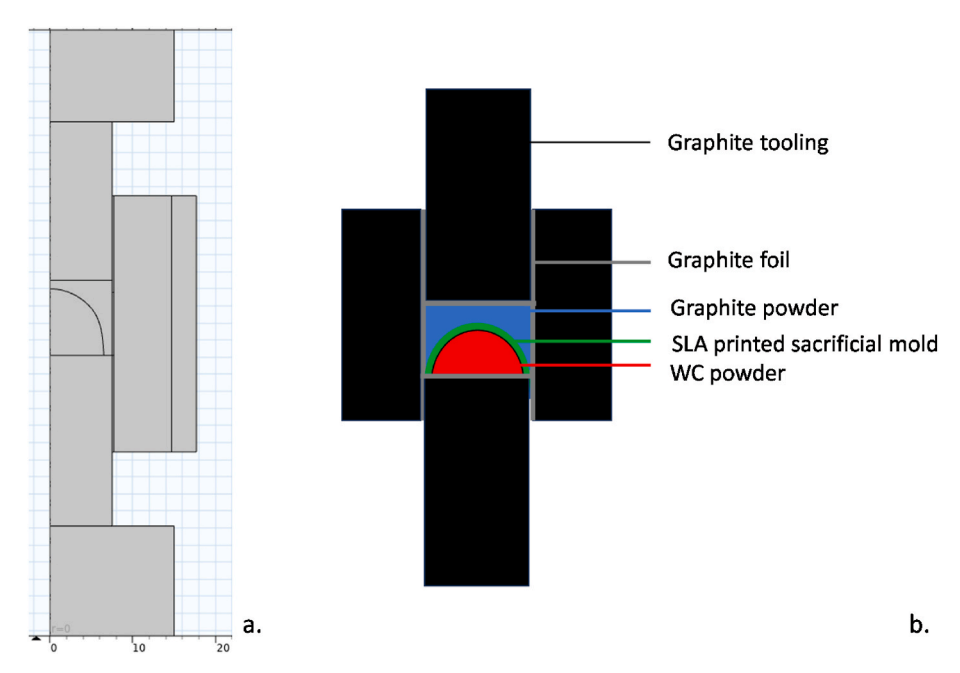


Fig. 17. Geometry for SPS 2D axis-symmetrical model of cupola sample (a.), schematic of the part preparation in a graphite die (b.).

sacrificial mold is required, created through the additive manufacturing method of stereolithography (SLA). The shape is smoothened by applying a coating of ethyl acetate. Subsequently, tungsten carbide powder is manually compacted into the mold, and the component is then placed into a graphite die filled with graphite powder, following the scheme illustrated in Fig. 17b [20,60]. The sacrificial powder utilized for this sintering process is graphite powder, expressly chosen to not sinter at relatively low temperatures [19]. Graphite powder proves to be an optimal choice as a sacrificial powder for carbides that should not be susceptible to carbon contamination, such as oxides. Additionally, it allows for the demolding of the sample without causing damage (see Fig. 18).

The removal of the stereolithography (SLA) mold occurs through evaporation before initiating the primary sintering cycle. During this phase, the pressure is maintained at the minimum level permissible by the Spark Plasma Sintering (SPS) system (17 MPa). Simultaneously, a low-temperature cycle, involving a gradual heating process up to 600 °C, is implemented to completely outgas the polymer from the die. Following the evaporation of the sacrificial mold, only graphite powder remains atop the tungsten carbide powder sample. Any residual traces of the sacrificial mold in the die manifest as carbon residuals, which do not impede the sintering of tungsten carbide. Subsequently, a temperature cycle of 1550 °C is applied for a duration of 15 min, following a heating rate of 50 °C/min, all under a continuous applied pressure of 50 MPa.

In addition to the experimental work, the developed sintering model is employed for the tungsten carbide sample, utilizing identical thermal and pressure cycles. All parameters previously outlined in the preceding section are maintained exactly as specified. The only subtle distinction lies in the geometry, as depicted in Fig. 17a, encompassing the shape of the initial cupola sample and its surrounding graphite sacrificial powder. The model effectively simulates the sintering process, encompassing the steps following the outgassing and removal of the resin mold. Moreover, the model accounts for the heating and compaction of the graphite powder, which does not undergo sintering at such temperatures, utilizing a cold isostatic pressing model [19].

After sintering, the sample exhibits a relative density of 95.2%, determined through the Archimede method. The final geometry of the sample features a base diameter of 12.30 mm and a sample height of 4.47 mm. In contrast, the simulation predicts a base diameter of 12.31 mm and a sample height of 4.55 mm, yielding a mean relative density of 95.6% (refer to Fig. 19).

In comparison to the cylindrical sample discussed in preceding sections, the current cupola sample experiences slight radial shrinkage due to the compaction of the surrounding graphite powder. This powder not

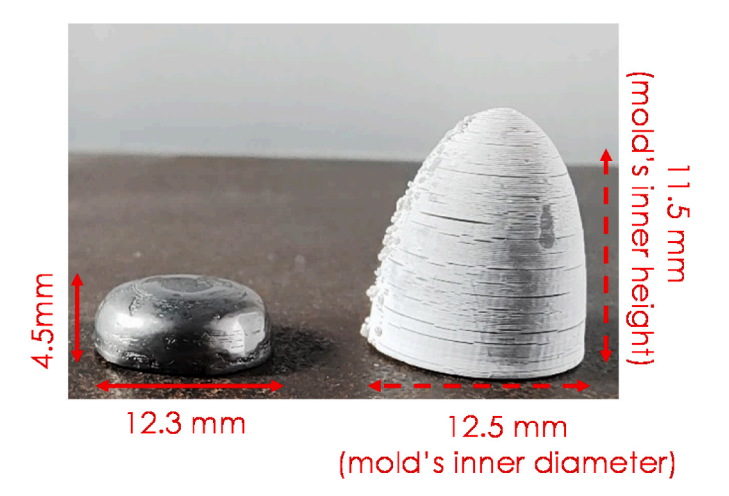


Fig. 18. Polished cupola sample (left) and its original SLA printed sacrificial mold smoothed with ethyl-acetate (right) with 1.5 mm mold thickness at the basis and 2 mm at the top.

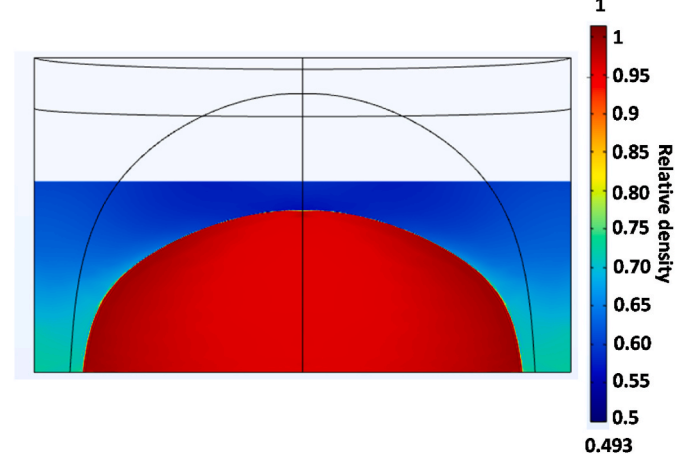


Fig. 19. Final relative density distribution for the cupola sample and its sacrificial compacted graphite powder (grey lines representing the initial geometry).

only applies a uniaxial pressure but also imparts a subtle lateral pressure. The model successfully captures the intricacies of this more complex scenario, incorporating a physics model for the cold pressing of graphite powder. Notably, the simulated graphite powder maintains a non-dense state, ranging from 45% relative density at the initial compacted state to an average of 63.5% relative density (see Fig. 19). Furthermore, the results of this study underscore multiple opportunities presented by integrating comprehensive modeling with the capability for producing complex shapes through additive manufacturing.

4. Conclusions

This article delves into the process of spark plasma sintering applied to tungsten carbide powder and its application for complex shape parts production via additive manufacturing method. The focus of this document is to compile comprehensive information regarding the study, spanning from the characterization of the powder to the creation of an elaborate finite element simulation for its sintering via SPS and its application to the production of dense complex shape. By enabling the design of complex-shaped sacrificial molds, AM plays a pivotal role in achieving intricate shaping for parts manufactured through SPS. Preliminary sintering cycles showed the great quality of the powder without any problematics of melting and thermal runaway and almost fully dense microstructure from simple thermal cycles at low temperature (1550 °C) and low pressure (50 MPa). Relatively low microstructural coarsening is also being observed from nanosized powder (104 nm mean grain size). Thus, reflecting the good quality of initial pure WC nano powder to achieve almost full density and a limited grain growth under these conditions.

The central theme of this document revolves around the methods employed to derive constitutive parameters based on the Skorohod-Olevsky theory of continuum sintering, grounded in the processing of experimental data. This includes the discussion of critical parameters identification such as the apparent sintering activation energy (800 kJ/mol) by the mean of different methods, creep law stress exponent (n = 4.0), and pre-exponential factor.

Furthermore, this report details the successful transfer of the developed model into a Multiphysics Finite Element Method (FEM) commercial software, COMSOL. This transition enables the integration of thermal, electrical, and mechanical physics for a comprehensive simulation of tungsten carbide spark plasma sintering. The model has proven to be highly predictive, offering insights into density and grain size distributions correlated with temperature gradients within the specimen. The article effectively concludes by affirming the applicability of

the developed model for both predicting and producing complex shapes through spark plasma sintering of tungsten carbide. It highlights the numerous opportunities arising from integrating advanced modeling with the capability to produce complex shapes through additive manufacturing.

CRediT authorship contribution statement

Thomas Grippi: Conceptualization, Software, Writing – original draft, Writing – review & editing. **Elisa Torresani:** Conceptualization, Methodology, Supervision, Writing – review & editing. **Andrii L. Maximenko:** Conceptualization, Supervision, Writing – review & editing. **Eugene A. Olevsky:** Conceptualization, Methodology, Software, Supervision, Validation, Writing – review & editing.

Declaration of competing interest

The authors declare that they have no known competing financial interests or personal relationships that could have appeared to influence the work reported in this paper.

Acknowledgements

The support of US Army DEVCOM - Army Research Laboratory (Contract W911-NF-20-2-0226) is gratefully appreciated. The support of the National Science Foundation ((Grants 1900876, 2138421, and 2119832)) is gratefully acknowledged.

References

- A.S. Kurlov, A.I. Gusev, A.A. Rempel, Int. Journal of Refractory Metals and hard materials Vacuum sintering of WC – 8 wt. % Co hardmetals from WC powders with different dispersity, RMHM 29 (2011) 221–231, https://doi.org/10.1016/j. iirmhm.2010.10.010.
- [2] A.F. Guillermet, Thermodynamic properties of the Co-W-C system, Metall. Trans. A 20 (1989) 935–956, https://doi.org/10.1007/BF02651660.
- [3] X. Yang, K. Wang, G. Zhang, K. Chou, Fabrication and Performances of WC-Co Cemented Carbide with a Low Cobalt Content, 2022, pp. 1341–1353, https://doi. org/10.1111/jiac.13966.
- [4] Y.M.Y. Kanemitsu, T. Nishimura, H. Yoshino, K. Takao, Effect of hot isostatic pressing on binderless cemented carbide, Refract met. Hard, Mater. (1982) 66–68.
- [5] X.H. Yang, K.F. Wang, G.H. Zhang, K.C. Chou, Fabrication and performances of WC-Co cemented carbide with a low cobalt content, Int. J. Appl. Ceram. Technol. 19 (2022) 1341–1353, https://doi.org/10.1111/ijac.13966.
- [6] A. V Samokhin, N. V Alekseev, S.A. Kornev, M.A. Sinaiskii, A. V Kolesnikov, Tungsten Carbide and Vanadium Carbide Nanopowders Synthesis in DC Plasma Reactor, 2013, pp. 605–616, https://doi.org/10.1007/s11090-013-9445-9.
- [7] S. Grasso, J. Poetschke, V. Richter, G. Maizza, Y. Sakka, M.J. Reece, Low-temperature spark plasma sintering of pure nano WC powder, J. Am. Ceram. Soc. 96 (2013) 1702–1705, https://doi.org/10.1111/jace.12365.
- [8] J. Sun, J. Zhao, Z. Huang, K. Yan, X. Shen, J. Xing, Y. Gao, Y. Jian, H. Yang, B. Li, A Review on Binderless Tungsten Carbide: Development and Application, 2020, https://doi.org/10.1007/s40820-019-0346-1.
- [9] A. Gubernat, P. Rutkowski, G. Grabowski, D. Zientara, Hot pressing of tungsten carbide with and without sintering additives, Int. J. Refract. Met. Hard Mater. 43 (2014) 193–199, https://doi.org/10.1016/j.ijrmhm.2013.12.002.
- [10] X. Wei, C. Back, O. Izhvanov, O.L. Khasanov, C.D. Haines, E.A. Olevsky, Spark plasma sintering of commercial zirconium carbide powders: densification behavior and mechanical properties, Materials 8 (2015) 6043–6061, https://doi.org/ 10.3390/ma8095289.
- [11] D. Lahiri, E. Khaleghi, S.R. Bakshi, W. Li, E.A. Olevsky, A. Agarwal, Grapheneinduced strengthening in spark plasma sintered tantalum carbide-nanotube composite, Scripta Mater. 68 (2013) 285–288, https://doi.org/10.1016/j. scriptamat.2012.10.043.
- [12] E.A. Olevsky, C. Garcia-Cardona, W.L. Bradbury, C.D. Haines, D.G. Martin, D. Kapoor, Fundamental aspects of spark plasma sintering: II. Finite element analysis of scalability, J. Am. Ceram. Soc. 95 (2012) 2414–2422, https://doi.org/ 10.1111/j.1551-2916.2012.05096.x.
- [13] E.A. Olevsky, D.V. Dudina, Field-Assisted Sintering, Springer International Publishing, Cham, 2018, https://doi.org/10.1007/978-3-319-76032-2.
 [14] Z.A. Munir, U. Anselmi-Tamburini, M. Ohyanagi, The effect of electric field and
- [14] Z.A. Munir, U. Anselmi-Tamburini, M. Ohyanagi, The effect of electric field and pressure on the synthesis and consolidation of materials: a review of the spark plasma sintering method, J. Mater. Sci. 41 (2006) 763–777, https://doi.org/ 10.1007/s10853-006-6555-2.
- [15] Z.A. Munir, D.V. Quach, M. Ohyanagi, Electric current activation of sintering: a review of the pulsed electric current sintering process, J. Am. Ceram. Soc. 94 (2011) 1–19, https://doi.org/10.1111/j.1551-2916.2010.04210.x.

- [16] X. Li, D. Jiang, J. Zhang, Q. Lin, Z. Chen, Z. Huang, Densification behavior and related phenomena of spark plasma sintered boron carbide, Ceram. Int. 40 (2014) 4359–4366, https://doi.org/10.1016/j.ceramint.2013.08.106.
- [17] D. Giuntini, J. Raethel, M. Herrmann, A. Michaelis, E.A. Olevsky, Advancement of tooling for spark plasma sintering, J. Am. Ceram. Soc. 98 (2015) 3529–3537, https://doi.org/10.1111/jace.13528.
- [18] C. Manière, E. Torresani, E.A. Olevsky, Simultaneous spark plasma sintering of multiple complex shapes, Materials 12 (2019) 1–14, https://doi.org/10.3390/ ma12040557.
- [19] E. Torresani, M. Carrillo, C. Haines, D. Martin, E. Olevsky, Fabrication of powder components with internal channels by spark plasma sintering and additive manufacturing, J. Eur. Ceram. Soc. 43 (2022) 1117–1126, https://doi.org/ 10.1016/j.jeurceramsoc.2022.11.008.
- [20] C. Manière, E. Nigito, L. Durand, A. Weibel, Y. Beynet, C. Estournès, Spark plasma sintering and complex shapes: the deformed interfaces approach, Powder Technol. 320 (2017) 340–345, https://doi.org/10.1016/j.powtec.2017.07.048.
- [21] C. Manière, L. Durand, A. Weibel, G. Chevallier, C. Estournès, A sacrificial material approach for spark plasma sintering of complex shapes, Scripta Mater. 124 (2016) 126–128, https://doi.org/10.1016/j.scriptamat.2016.07.006.
- [22] E.A. Olevsky, Theory of sintering: from discrete to continuum, Mater. Sci. Eng. R Rep. 23 (1998) 41–100, https://doi.org/10.1016/S0927-796X(98)00009-6.
- [23] C. Van Nguyen, S.K. Sistla, S. Van Kempen, N.A. Giang, A. Bezold, C. Broeckmann, F. Lange, A comparative study of different sintering models for Al2O3, J. Ceram. Soc. Japan. 124 (2016) 301–312. https://www.jstage.jst.go.jp/article/jcersj2/124/4/124 15257/ article/-char/ja/.
- [24] C. Manière, C. Harnois, S. Marinel, Porous stage assessment of pressure assisted sintering modeling parameters: a ceramic identification method insensitive to final stage grain growth disturbance, Acta Mater. 211 (2021), https://doi.org/10.1016/ j.actamat.2021.116899.
- [25] B. Sarbandi, J. Besson, M. Boussuge, D. Ryckelynck, F. Barlat, Y.H. Moon, M.G. Lee, Anisotropic Constitutive Model and FE Simulation of the Sintering Process of Slip Cast Traditional Porcelain, 2010, pp. 689–696, https://doi.org/10.1063/ 1.3457622.
- [26] T. Kraft, H. Riedel, Numerical simulation of solid state sintering; model and application, J. Eur. Ceram. Soc. (2004), https://doi.org/10.1016/S0955-2219(03) 00222-X
- [27] R.K. Bordia, R. Zuo, O. Guillon, S.M. Salamone, J. Rödel, Anisotropic constitutive laws for sintering bodies, Acta Mater. 54 (2006) 111–118, https://doi.org/ 10.1016/j.actamat.2005.08.025.
- [28] O. Gillia, D. Bouvard, Phenomenological analysis of densification kinetics during sintering: application to WC-Co mixture, Mater. Sci. Eng. (2000), https://doi.org/ 10.1016/S0921-5093(99)00621-8.
- [29] C. Mani, C. Harnois, S. Marinel, Journal of the European Ceramic Society Role of Microstructure Reactivity and Surface Diffusion in Explaining Flash (Ultra-rapid) Sintering Kinetics, vol. 43, 2023, pp. 2057–2068, https://doi.org/10.1016/j. jeurceramsoc.2022.12.006.
- [30] W. Li, E.A. Olevsky, J. McKittrick, A.L. Maximenko, R.M. German, Densification mechanisms of spark plasma sintering: multi-step pressure dilatometry, J. Mater. Sci. 47 (2012) 7036–7046, https://doi.org/10.1007/s10853-012-6515-y.
- [31] G. Lee, C. Manière, J. McKittrick, E.A. Olevsky, Electric current effects in spark plasma sintering: from the evidence of physical phenomenon to constitutive equation formulation, Scripta Mater. 170 (2019) 90–94, https://doi.org/10.1016/ iscriptamat 2019 05 040
- [32] S.J. Park, P. Suri, E. Olevsky, R.M. German, Master sintering curve formulated from constitutive models, J. Am. Ceram. Soc. 92 (2009) 1410–1413, https://doi.org/ 10.1111/j.1551-2916.2009.02983.x.
- [33] T. Grippi, S. Béhar-Lafenetre, H. Friedrich, D. Haas, U. Schenderlein, S. Marinel, C. Manière, Grain growth modeling for gas pressure sintering of silicon nitride based ceramics, Mater. Today Commun. 34 (2023), https://doi.org/10.1016/j. mtcomm. 2022.105189
- [34] N. Ku, J.J.P. Iii, S. Kilczewski, Additive manufacturing of cemented tungsten carbide with a cobalt-free alloy binder by selective laser melting for high-hardness applications, JOM 71 (2019) 1535–1542, https://doi.org/10.1007/s11837-019-02366.2
- [35] R.M. German, German, Sintering Theory and Practice, Chapitre, 1996.
- [36] S.K. Sun, G.J. Zhang, W.W. Wu, J.X. Liu, J. Zou, T. Suzuki, Y. Sakka, Reactive spark plasma sintering of binderless WC ceramics at 1500 C, Int. J. Refract. Met. Hard Mater. 43 (2014) 42–45, https://doi.org/10.1016/j.ijrmhm.2013.10.013.
- [37] L. Sun, C.C. Jia, M. Xian, A research on the grain growth of WC-Co cemented carbide, Int. J. Refract. Met. Hard Mater. 25 (2007) 121–124, https://doi.org/ 10.1016/j.ijrmhm.2006.03.002.
- [38] V.V. Skorohod, Rheological basis of the theory of sintering, Nauk. Dumka, Kiev (1972).
- [39] C. Manière, J. Sambasene, C. Harnois, C. Couder, C. Bilot, S. Marinel, Mechanics of Materials Pressure Assisted Sintering Stress Exponent Assessment Methods: Accuracy Analysis and Effect of Sintering Stress, 2023, p. 181, https://doi.org/ 10.1016/j.mechmat.2023.104664.
- [40] J.T. Smith, J.D. Wood, Elevated Temperature Compressive Creep Behavior of Tungsten Carbide-Cobalt Alloys, 1968.
- [41] S. Lay, J. Vicens, F. Osterstock, High temperature creep of WC-Co alloys, J. Mater. Sci. 22 (1987) 1310–1322, https://doi.org/10.1007/BF01233127.
- [42] T. Grippi, S. Béhar-Lafenêtre, H. Friedrich, D. Haas, U. Schenderlein, S. Marinel, C. Manière, Densification modeling for gas pressure sintered silicon nitride-based ceramics with Thermo-Optical dilatometry, J. Eur. Ceram. Soc. (2023), https://doi. org/10.1016/j.jeurceramsoc.2023.09.028.

- [43] J. Wang, R. Raj, Estimate of the activation energies for boundary diffusion from rate-controlled sintering of pure alumina, and alumina doped with zirconia or titania, J. Am. Ceram. Soc. 73 (1990) 1172–1175, https://doi.org/10.1111/j.1151-2916.1990.tb05175.x.
- [44] F. Raether, P. Schulze Horn, Investigation of sintering mechanisms of alumina using kinetic field and master sintering diagrams, J. Eur. Ceram. Soc. 29 (2009) 2225–2234, https://doi.org/10.1016/j.jeurceramsoc.2009.01.025.
- [45] C. Manière, T. Grippi, S. Marinel, Estimate microstructure development from sintering shrinkage: a kinetic field approach, Mater. Today Commun. 31 (2022), https://doi.org/10.1016/j.mtcomm.2022.103269.
- [46] V.N. Chuvil'deev, Y.V. Blagoveshchenskiy, A.V. Nokhrin, M.S. Boldin, N. V. Sakharov, N.V. Isaeva, S.V. Shotin, O.A. Belkin, A.A. Popov, E.S. Smirnova, E. A. Lantsev, Spark plasma sintering of tungsten carbide nanopowders obtained through DC arc plasma synthesis, J. Alloys Compd. 708 (2017) 547–561, https://doi.org/10.1016/i.iallcom.2017.03.035.
- [47] G. Lee, J. McKittrick, E. Ivanov, E.A. Olevsky, Densification mechanism and mechanical properties of tungsten powder consolidated by spark plasma sintering, Int. J. Refract. Met. Hard Mater. 61 (2016) 22–29, https://doi.org/10.1016/j. ijrmhm.2016.07.023.
- [48] M.S. Kovalchenko, Pressure sintering kinetics of tungsten and titanium carbides, Int. J. Refract. Met. Hard Mater. 39 (2013) 32–37, https://doi.org/10.1016/j. ijrmhm.2013.03.001.
- [49] H. Su, D.L. Johnson, Master sintering curve: a practical approach to sintering, J. Am. Ceram. Soc. 79 (1996) 3211–3217, https://doi.org/10.1111/j.1151-2916.1996.tb08097.x.
- [50] J.A. Wurst, J.C., Nelson, Lineal intercept method for measuring grain size in twophase polycrystalline ceramics, J. Am. Ceram. Soc. (1972) 55–109.
- [51] J. Besson, M. Abouaf, Rheology of porous alumina and simulation of hot isostatic pressing, J. Am. Ceram. Soc. (1992), https://doi.org/10.1111/j.1151-2916.1992. tb04479.x.

- [52] C. Manière, J.S. Diatta, C. Couder, C. Harnois, S. Marinel, Spark plasma sintering grain growth assessment by densification kinetics analysis, Scripta Mater. 228 (2023), https://doi.org/10.1016/j.scriptamat.2023.115346.
- [53] J. Diatta, G. Antou, N. Pradeilles, A. Maître, Numerical modeling of spark plasma sintering—discussion on densification mechanism identification and generated porosity gradients, J. Eur. Ceram. Soc. 37 (2017) 4849–4860, https://doi.org/ 10.1016/j.jeurceramsoc.2017.06.052.
- [54] J. Diatta, E. Torresani, A. Maximenko, C. Haines, D. Martin, E. Olevsky, Peltier effect during spark plasma sintering of boron carbide, Results Phys. 29 (2021) 104719, https://doi.org/10.1016/j.rinp.2021.104719.
- [55] C. Manière, L. Durand, E. Brisson, H. Desplats, P. Carré, P. Rogeon, C. Estournès, Contact resistances in spark plasma sintering: from in-situ and ex-situ determinations to an extended model for the scale up of the process, J. Eur. Ceram. Soc. 37 (2017) 1593–1605, https://doi.org/10.1016/j.jeurceramsoc.2016.12.010.
- [56] C. Manière, G. Lee, E.A. Olevsky, Proportional integral derivative, modeling and ways of stabilization for the spark plasma sintering process, Results Phys. 7 (2017) 1494–1497, https://doi.org/10.1016/j.rinp.2017.04.020.
- [57] H. Tripathy, C. Sudha, V.T. Paul, R. Thirumurugesan, T.N. Prasanthi, R. Sundar, N. Vijayashanthi, P. Parameswaran, S. Raju, High temperature thermophysical properties of spark plasma sintered tungsten carbide, Int. J. Refract. Met. Hard Mater. 104 (2022) 105804, https://doi.org/10.1016/j.ijrmhm.2022.105804.
- [58] V. Kazymyrovych, V. Kryzhanivskyy, International journal of refractory metals and hard materials thermal properties of cemented carbides used for metal cutting, Int. J. Refract. Met. Hard Mater. 111 (2023) 106097, https://doi.org/10.1016/j. iirmbm. 2022 166007
- [59] X. Wei, D. Giuntini, A.L. Maximenko, C.D. Haines, E.A. Olevsky, Experimental investigation of electric contact resistance in spark plasma sintering tooling setup, J. Am. Ceram. Soc. 98 (2015) 3553–3560, https://doi.org/10.1111/jace.13621.
- [60] C. Manière, G. Lee, E.A. Olevsky, Flash sintering of complex shapes, Appl. Mater. Today 26 (2022), https://doi.org/10.1016/j.apmt.2021.101293.